

Zhang, Z., and Nie, J., 2024, Anti-phase variation of long eccentricity and precipitation in inland Asia during the middle Miocene Climatic Optimum: GSA Bulletin, <https://doi.org/10.1130/B37333.1>.

Supplemental Material

Table S1: Detrital apatite fission track (ATF) data from the QN section.

Table S2: Detrital apatite (U-Th)/He data from the QN section.

Table S3: Carbonate U-Pb data from the QN section.

Table S4: Detrital zircon U-Pb data from the QN section.

Table S5: Magnetostratigraphy data from the QN section.

Table S6: The time series environmental magnetic records from the QN section.

Table S7: The Earth Orbital Parameters for simulation.

SuppText1: Lithology and depositional environment of the QN section and Supplementary Figures S1-S14.

Figure S1. Zijdeveld (Zijdeveld, 1967), equal area projection and normalized intensity variation plots of representative samples from the QN section.

Figure S2. Magnetostratigraphic jackknife analysis (Tauxe and Gallet, 1991) for the QN section.

Figure S3. Recurrence analysis of χ_{fd} /HIRM records from the QN section.

Figure S4. χ_{fd} /HIRM records and sampling interval statistics for this study.

Figure S5. A potential old-age correlation of the geomagnetic polarity timescale from the QN section with GPTS.

Figure S6. Four alternative correlations of the observed magnetic polarities of the QN section with the Geomagnetic polarity time scale (GPTS) (Ogg, 2020) based on “correlation costs” using dynamic time warping algorithm (Lallier et al., 2013).

Figure S7. Power spectra of χ_{fd} /HIRM records for four age models.

Figure S8. Lithology and magnetic parameter records of the QN section on a depth scale.

Figure S9. Continuous wavelet transforms (Grinsted et al., 2004) of inland Asia paleoclimate records.

Figure S10. Environmental magnetic parameter variations of QN section during the middle Miocene.

Figure S11. Cross-spectral analyses between insolation and paleoclimate records in inland Asia during the MMCO (14-17 Ma).

Figure S12. Paleogeographic reconstruction used in the middle Miocene simulations (Poblete et al., 2021).

Figure S13. Changes in mean annual precipitation (shaded, mmday^{-1}) in response to Earth's orbit eccentricity.

Figure S14. Changes in summer precipitation (shaded, mmday^{-1}) in response to Earth's orbit eccentricity.

SuppText2: U-Pb zircon dating methods at CEREGE (2022-2023)

Anti-phase variation of long eccentricity and precipitation in inland Asia during the middle Miocene Climatic Optimum

Zhongbao Zhang^{1,2}, Junsheng Nie^{3,*}, Alexis Licht², Nathan Cogne⁴, Anta-Clarisse Sarr⁵, Tiantian Shen¹, Xingwan Liu¹, Weihang Wang¹, Peng Gao¹, Lin Li⁶, Marc Poujol⁴, Abel Guihou², Pierre Deschamps², Lewei Hao⁷

¹Ministry of Education Key Laboratory of Western China's Environmental Systems, College of Earth and Environmental Sciences, Lanzhou University, Lanzhou 730000, China

²Aix Marseille Univ, CNRS, IRD, INRAE, CEREGE, Aix-en-Provence, France

³School of Earth Sciences, Lanzhou University, Lanzhou 73000, China

⁴Univ Rennes, CNRS, Géosciences Rennes, UMR 6118, 35000 Rennes, France

⁵Univ. Grenoble Alpes, Univ. Savoie Mont-Blanc, CNRS, IRD, ISTerre, 38000 Grenoble, France

⁶Department of Geosciences, University of Arizona, Tucson, Arizona, USA

⁷Key Laboratory of Petroleum Resources, Northwest Institute of Eco-Environment and Resources, Chinese Academy of Sciences, Lanzhou 730000, China

***Corresponding author**

20

21

22

23 **Contents of this file**

24 Lithology and depositional environment.

25 Supplementary Figure S1-S14

26

27 **Introduction**

28 This supporting information provides a detailed description of the lithology, depositional
29 environment, and the Supplementary Figures S1-S14 for the main article.

30

Lithology and depositional environment

Based on the field lithology log, four distinct lithostratigraphic units for the QN section have been divided (Fig. 3).

The 0-425 m of the QN section primarily consists of thick layers of light brown to gray-green mudstone and green sandy mudstone and siltstone interlayers, with a series of gypsum layers within the siltstones. The upper part of this unit features abundant interbeds of brownish to gray-green mudstone and sandstone. Mudstone beds typically range from 1-20 m thick (up to ~70 m), characterized by fining-upward successions and often capped with greyish-green siltstones. Sandstones display dark gray mottling, planar-bedding and cross-stratifications, with a thickness ranging from 1-2 m. Gypsum layers exhibit a laminated distribution within the mudstone, with thickness ranging from 1 to 2 cm. This unit can be distinguished from other strata by its prominence of fine-grained deposits, and represents a low-energy lacustrine depositional environment.

The interval 425-711 m conformably overlies the underlying strata, and is dominated by red to green sandstones and siltstones, with light brown to gray-green mudstone interlayers. The sandstones form massive thick tabular beds, ranging in thickness from 1 to 15 m (up to ~60 m), with trough-cross bedding and erosive bases observed in the coarser deposits. Mudstone layers are homogeneous and massive, with a thickness of 1-7 m. Gypsum layers are 1-2 cm thick and distributed through the unit. This unit is characterized by abundant brownish red to gray-green medium-coarse sandstones, and displays a distinct upward coarsening and thickening trend, indicating a higher-energy deltaic depositional environment.

53 The strata from 711-887 m in the section conformably overlie the underlying layers,
54 primarily consisting of thick, massive mudstone ranging in color from brownish red to
55 gray-green, with minor interbeds of sandstone and gypsum. Mudstone layers are
56 homogeneous and massive, with a typically thickness of 1-20 m (up to ~60 m). Sandstone
57 interlayers are 1-3 m thick and gray-green in color, with trough-cross bedding and erosive
58 bases. The gypsum layers are 1-2 cm thick and distributed within the mudstones. This unit
59 is characterized by thick layers of brown to brick-red mudstones interbedded with thin
60 grayish-green mudstones. These depositional features suggest that this unit was deposited
61 in a low-energy shallow lacustrine environment.

62 The 887-1167 m interval conformably overlies the underlying strata, containing red
63 to green sandstones, siltstones, and mudstones. This unit is characterized by abundant brick
64 red and gray-green sandstone interlayers and gypsum beds, with trough-cross bedding and
65 erosive bases observed in the coarser deposits. Mudstone beds range from 1 to 10 m thick,
66 with wave ripples and horizontal laminations. The sandstones and siltstones, typically
67 ranging in thickness from 1 to 15 m (up to ~30 m), display a distinct upward coarsening
68 and thickening trend, indicating a higher-energy deltaic depositional environment.

69 Detailed lithological descriptions reveal two distinct depositional environments
70 along the QN section: a lacustrine environment at depths of 0-425 m and 711-887 m, and
71 a deltaic environment at depths of 425-711 m and 887-1167 m (Fig. 3). The depositional
72 environment of the QN section is highly dependent on the hydrological budget of the
73 Qaidam Basin, as it is situated on its northern edge and far from the Cenozoic depocenters
74 (Yin et al., 2008). The transition from a lacustrine to a deltaic depositional environment
75 around 425 m corresponds to an increase in precipitation seen in our humidity proxy (Fig.

S8). We speculate that increased precipitation intensified erosion, leading to the transportation and deposition of coarser sediments towards the lake margins, resulting in a transition of the depositional environment from lacustrine to deltaic. The persistent high precipitation and significant sediment transport into the lake during the MMCO likely caused a rise in lake levels, leading to the inundation of the delta and a lacustrine transgression (711-887 m). At the timing corresponding to deposits at around 887 m, precipitation gradually decreased (Fig. S8), while evaporation intensified, as evidenced by the frequent occurrence of gypsum layers (Fig. 9). This likely resulted in a decline in lake water levels, leading to a transition in the depositional environment from lacustrine to deltaic.

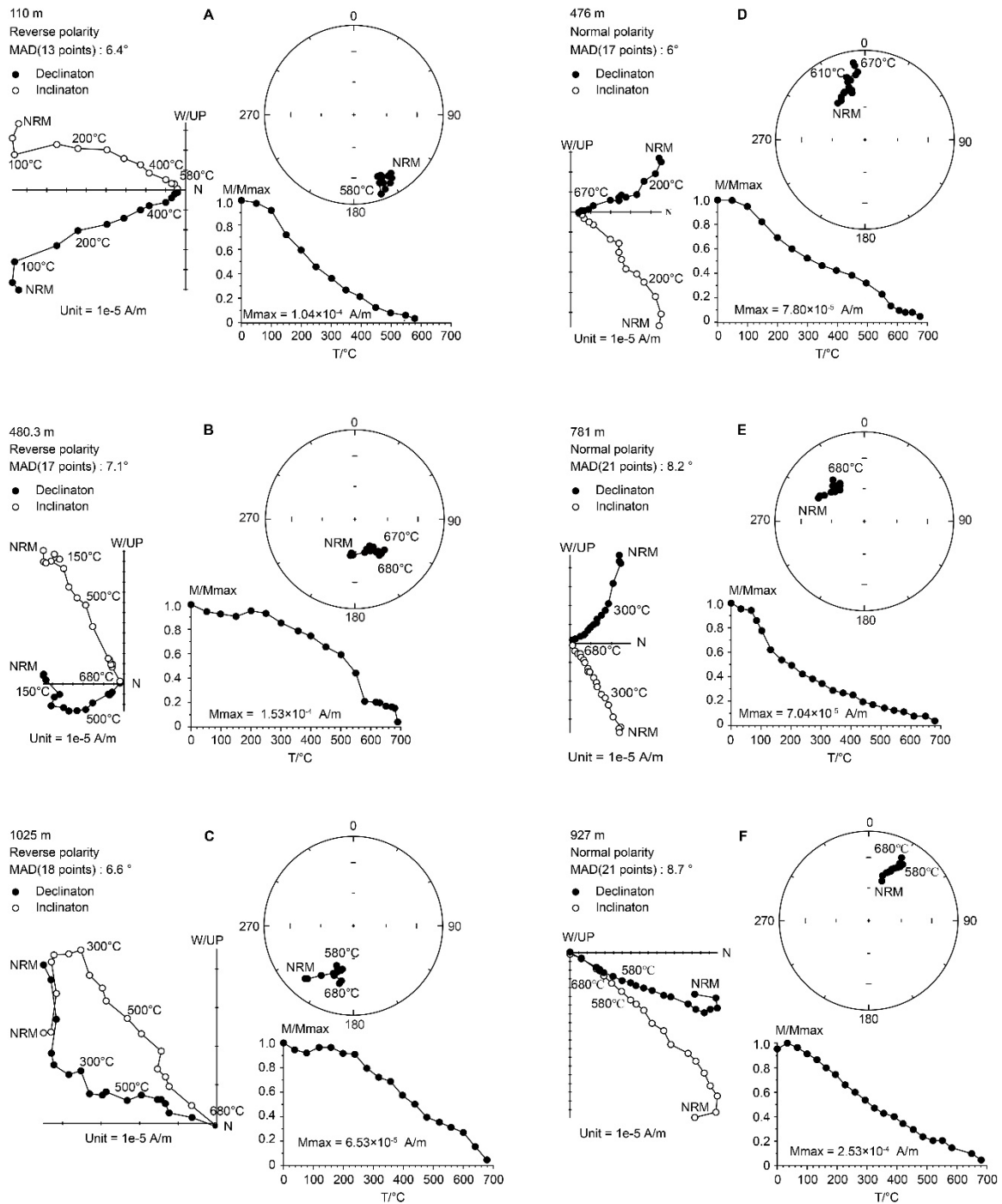


Figure S1. Zijderveld (Zijderveld, 1967), equal area projection and normalized intensity variation plots of representative samples from the QN section. (A, B, C) Reversed polarity zones. (D, E, F) Normal polarity zones.

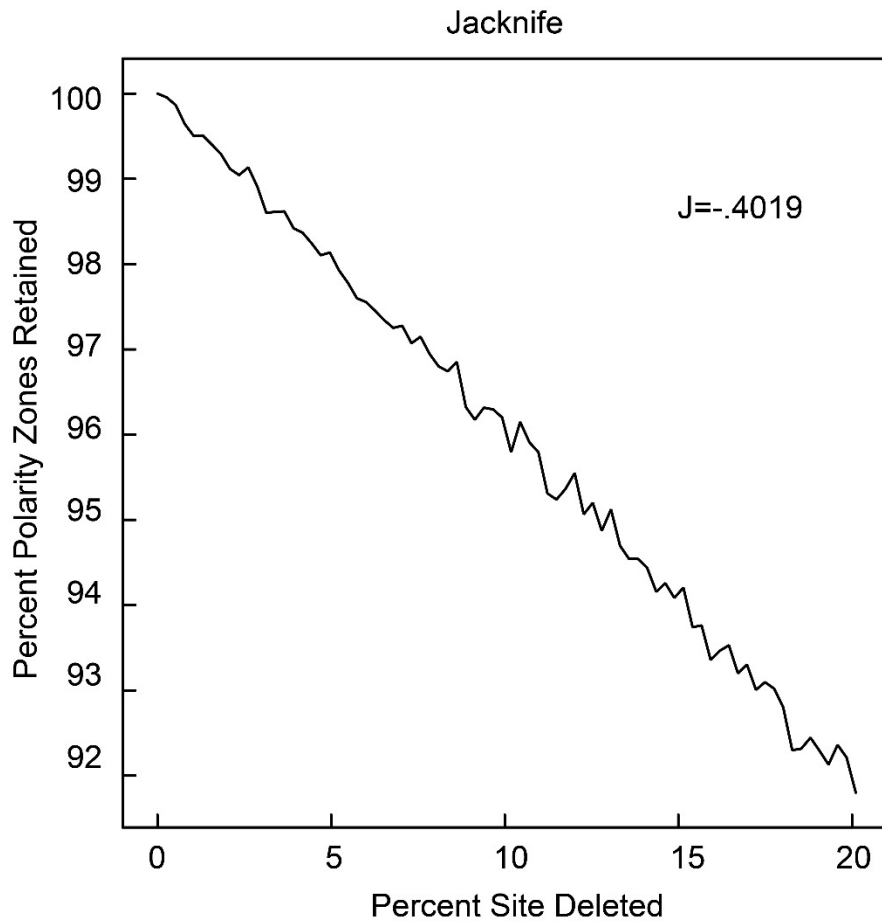


Figure S2. Magnetostratigraphic jackknife analysis (Tauxe and Gallet, 1991) for the QN section. The obtained slopes J have values of -0.4019 in the study section, indicating results of polarity intervals are robust for establishing magnetostratigraphy.

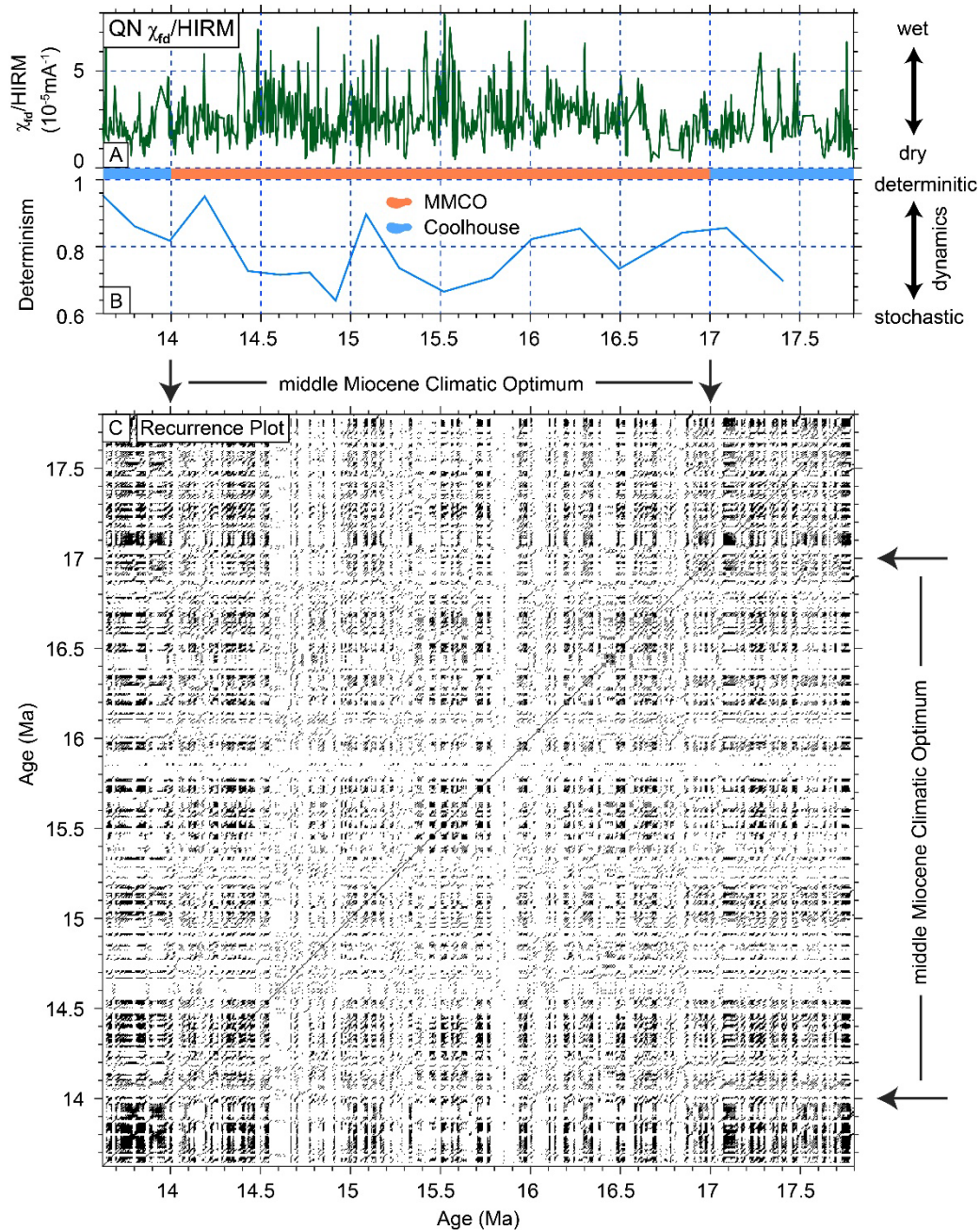


Figure S3. Recurrence analysis of $\chi_{fd}/HIRM$ records from the QN section. (A) $\chi_{fd}/HIRM$ records from QN section. (B) Recurrence analysis of determinism (DET). DET values near zero correspond to unpredictable dynamics, whereas large values indicate predictable dynamics. (C) Recurrence plot was created using $\chi_{fd}/HIRM$ records to compare climate change patterns within a certain interval to the entire record. Similar climate

dynamics will appear as dark areas in the plot, while dissimilar dynamics will appear as white.

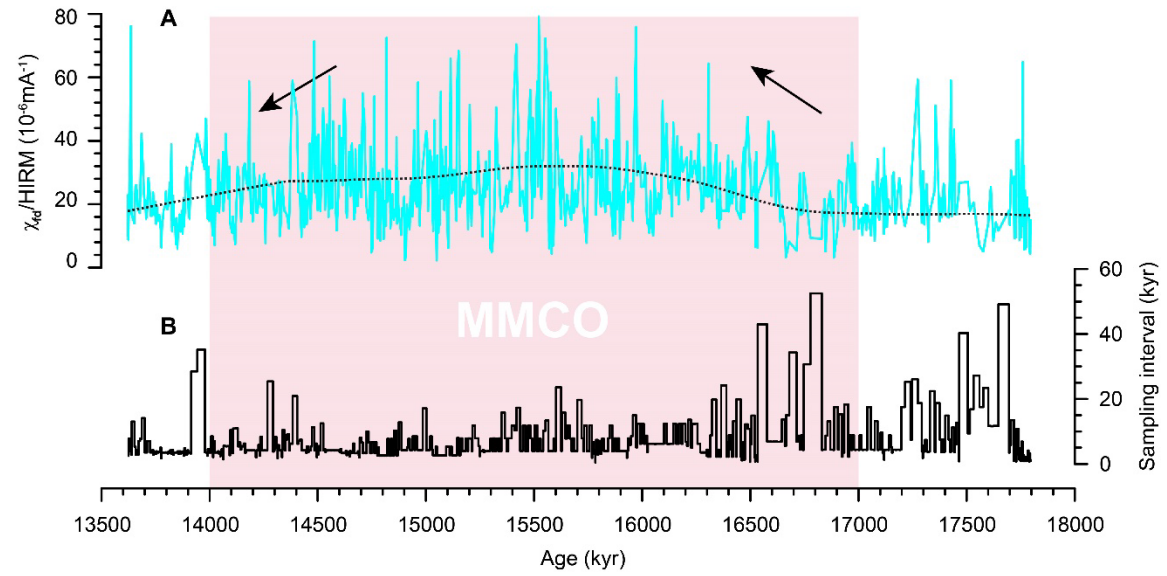


Figure S4. χ_{fd}/HIRM records and sampling interval statistics for this study. (A) χ_{fd}/HIRM record from the QN section and its Locally Weighted Scatterplot Smoothing with Robustness (LOWESS) result (black dashed line). (B) Sampling interval statistics for paleoclimate analysis.

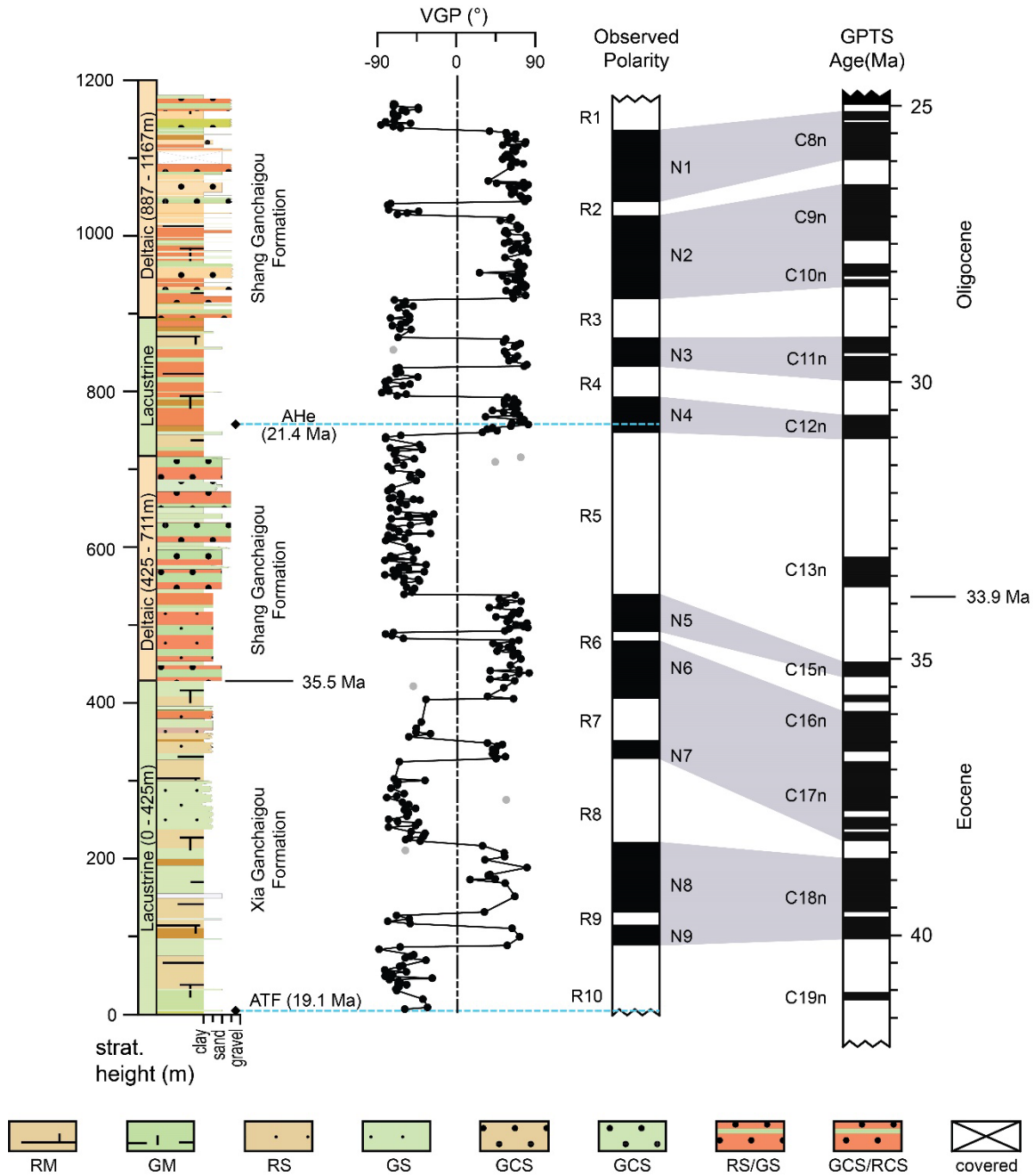
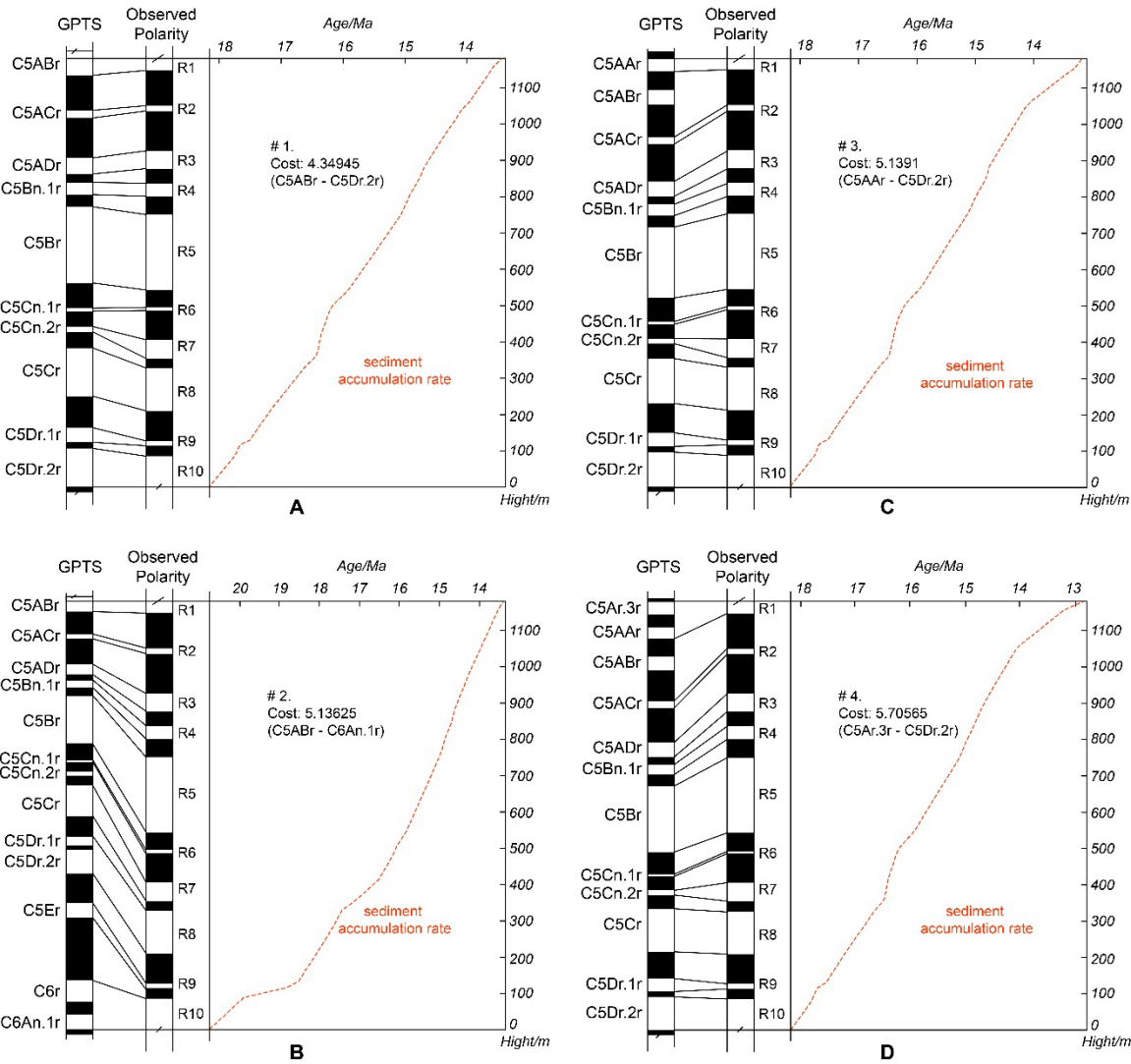


Figure S5. A potential old-age correlation of the geomagnetic polarity timescale from the QN section with GPTS. For caption, see figure 6. This correlation is based on the Eocene age explanation of the nucleus of Eboliang I Anticline. The blue dashed lines represent the youngest peak age constraints from detrital apatite low-temperature

thermochronology. ATF: apatite fission track. AHe: apatite (U-Th)/He dating. VGP: virtual geomagnetic polarity latitude, GPTS: Geomagnetic polarity time scale (Ogg, 2020).

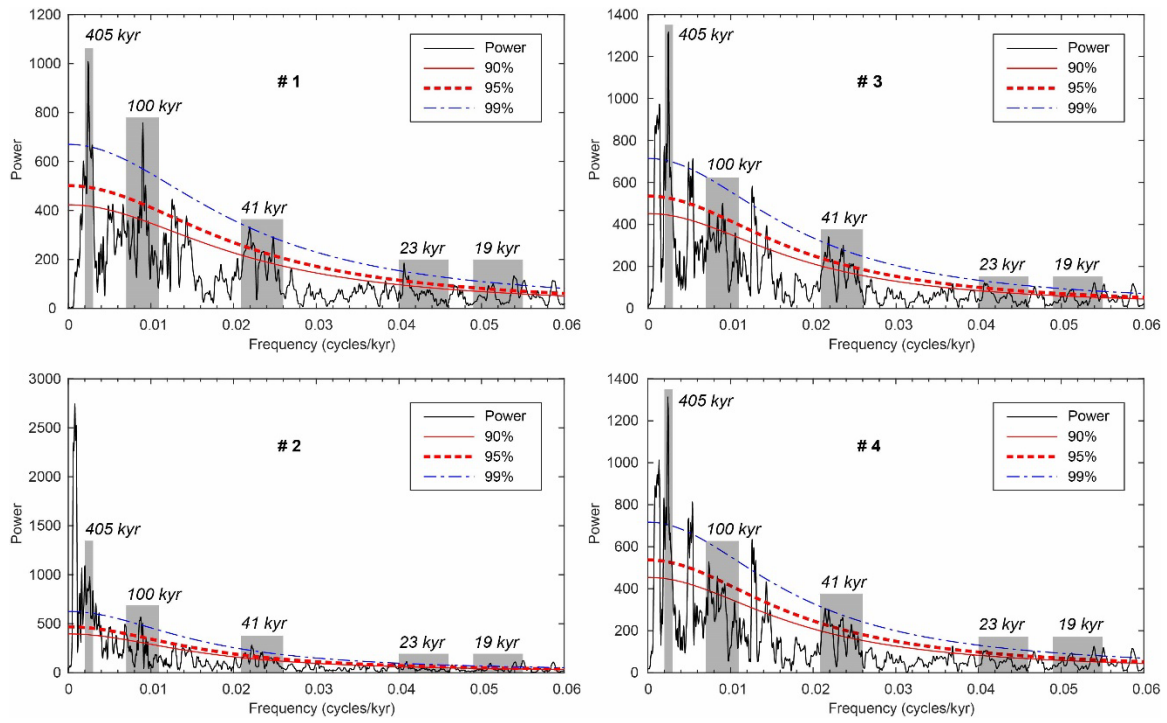
119



120

Figure S6. Four alternative correlations of the observed magnetic polarities of the QN section with the Geomagnetic polarity time scale (GPTS) (Ogg, 2020) based on "correlation costs" using dynamic time warping algorithm (Lallier et al., 2013). The least cost is considered the "best-fit correlations". A to D are listed in ascending order of cost. Age model A is the same as our paleomagnetic age model and shows the lowest cost.

126



127

128 **Figure S7. Power spectra of χ_{fd} /HIRM records for four age models. Results 1 to 4 are**
 129 **associated with four distinct cost scenarios presented in Figure S7.**

130

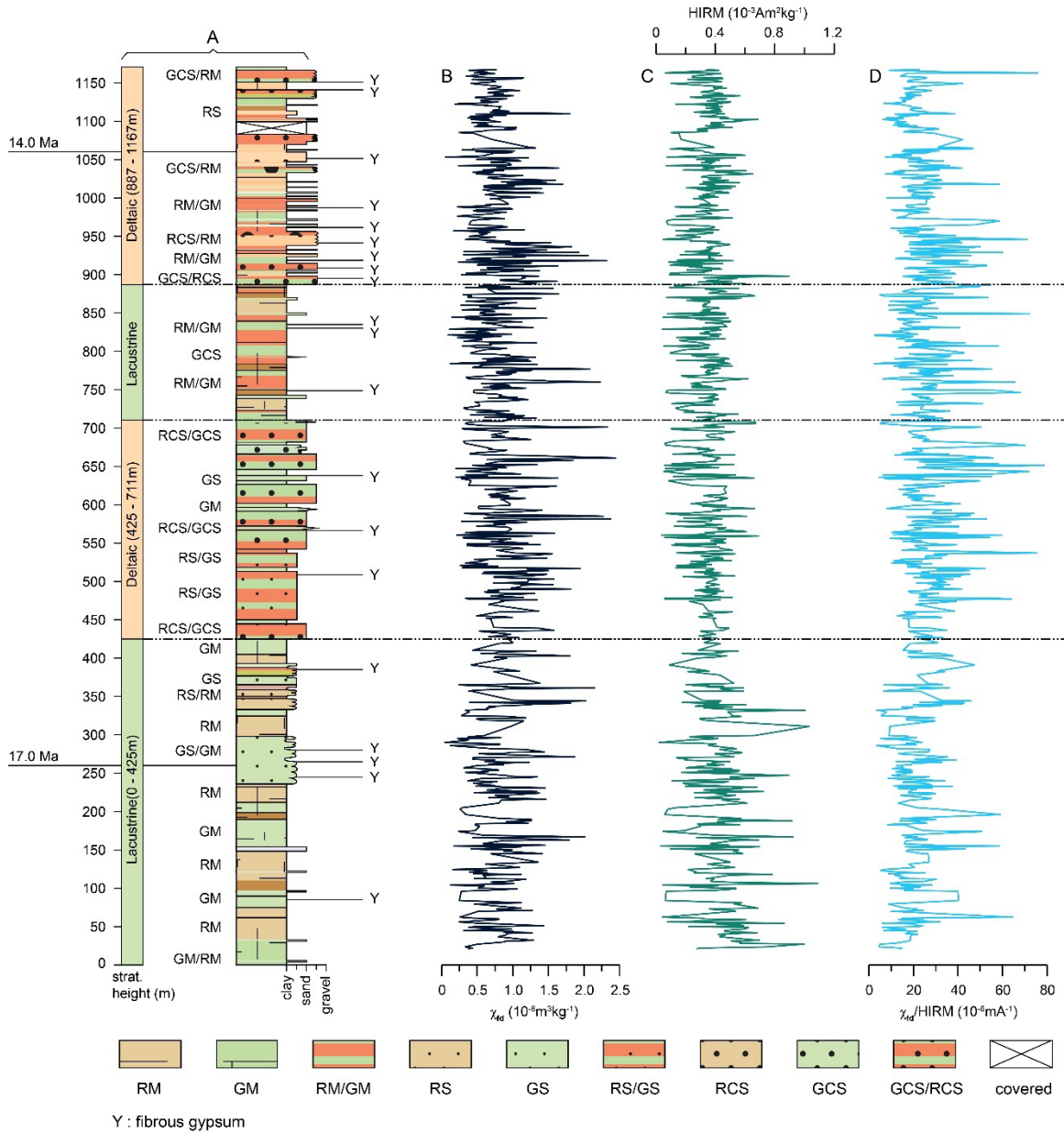
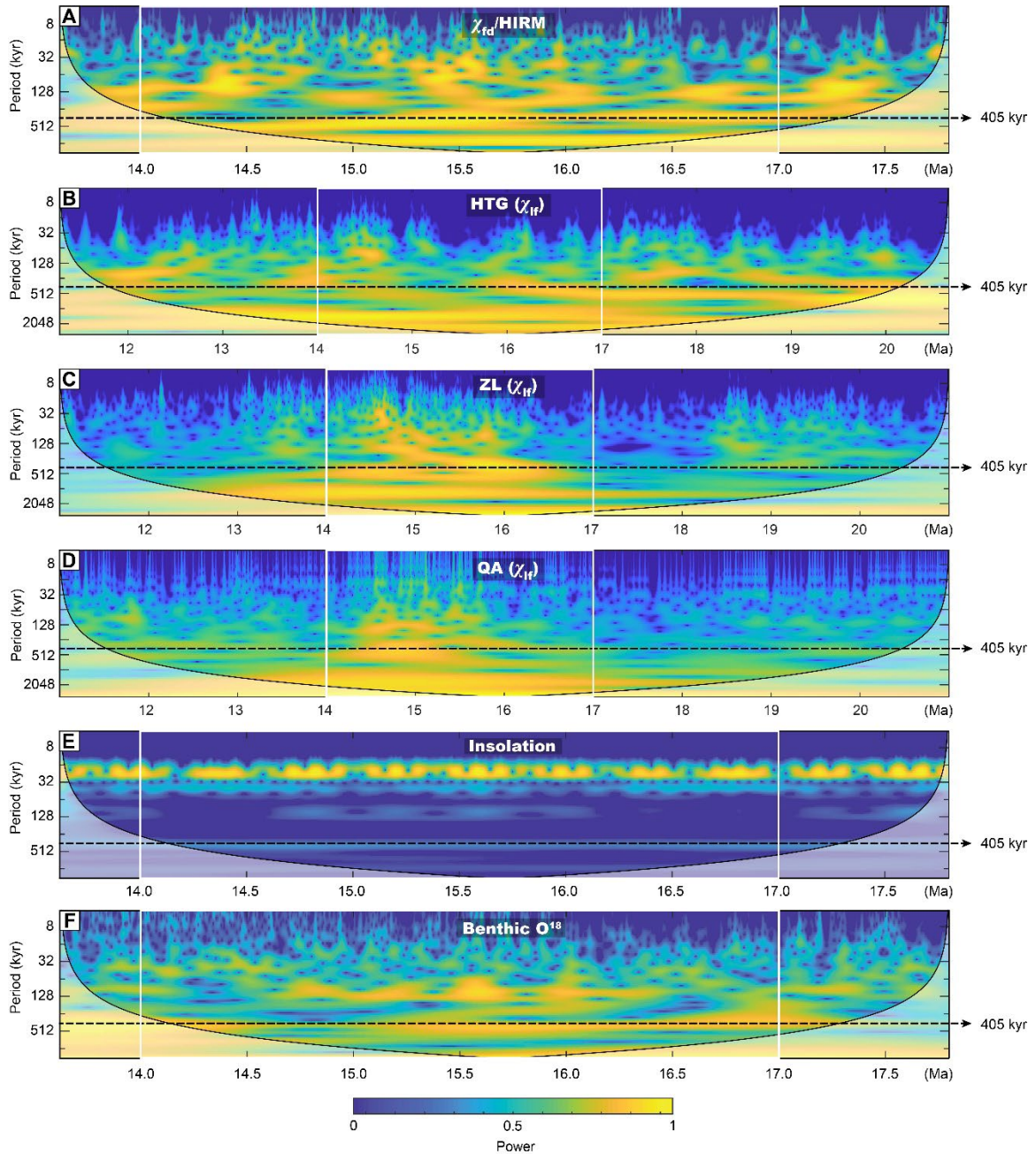


Figure S8. Lithology and magnetic parameter records of the QN section on a depth scale. (A) Lithology and depositional environment. (B) χ_{fd} (frequency-dependent magnetic susceptibility). (C) HIRM (hard isothermal remanent magnetization). (D) χ_{fd}/HIRM (frequency-dependent magnetic susceptibility/hard isothermal remanent magnetization). RM and GM, red and green mudstone; RS and GS, red and green sandstone; RCS and GCS,

137 red and green medium-coarse sandstone; RS/GS, Red and green sandstone interbeds;
 138 GCS/RCS, Red and green medium-coarse sandstone interbeds.

139



140

141 **Figure S9. Continuous wavelet transforms (Grinsted et al., 2004) of inland Asia**
 142 **paleoclimate records. (A, B) records from the Qaidam Basin and (C, D) records from the**

Chinese Loess Plateau. The records of (E and F) from 21 June insolation at 35° N (Laskar et al., 2004) and benthic $\delta^{18}\text{O}$ stack (Westerhold et al., 2020), respectively. The 405-kyr periodicity is labeled and indicated by the black dashed lines. The color scale indicates power, and which warm color indicates larger power. The shaded areas illustrate the cone of influence, where edge effects become important. HTG, Huatugou; ZL, Zhuanglang; QA, Qin'an.

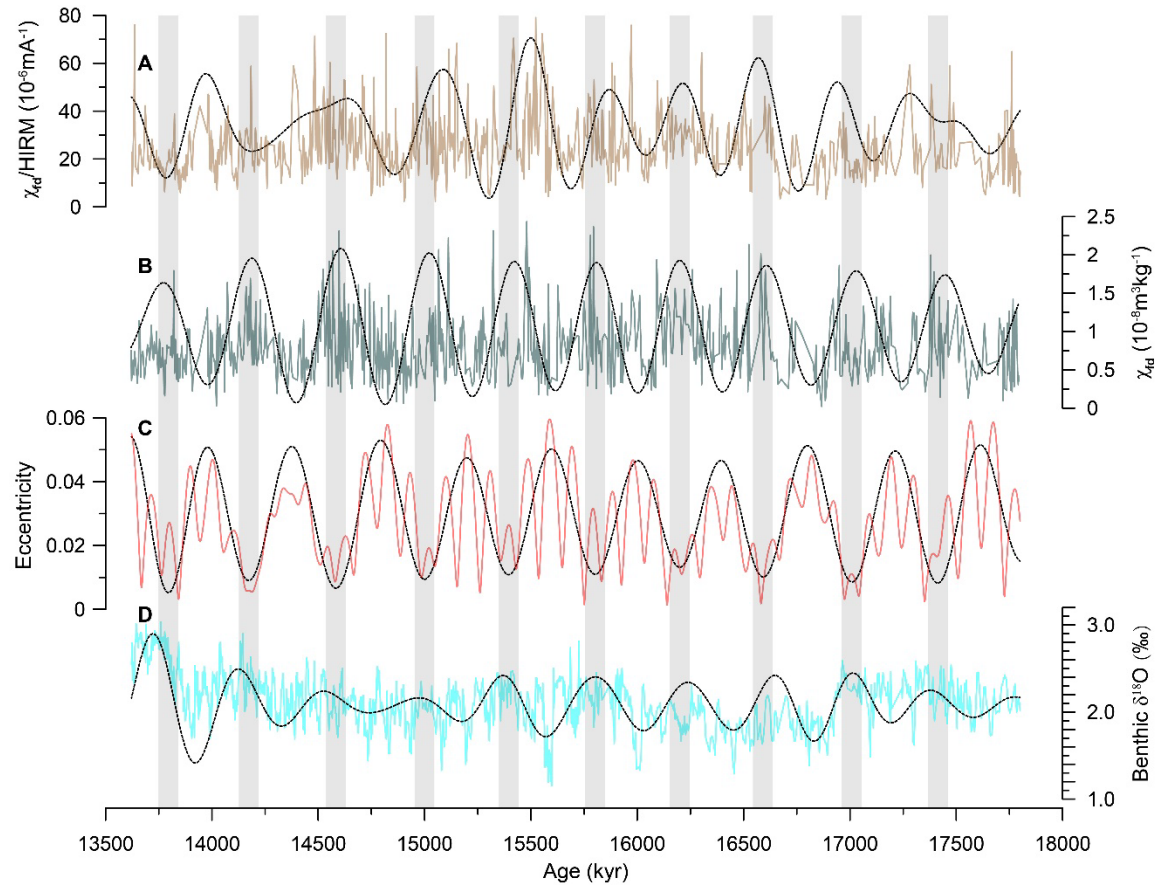
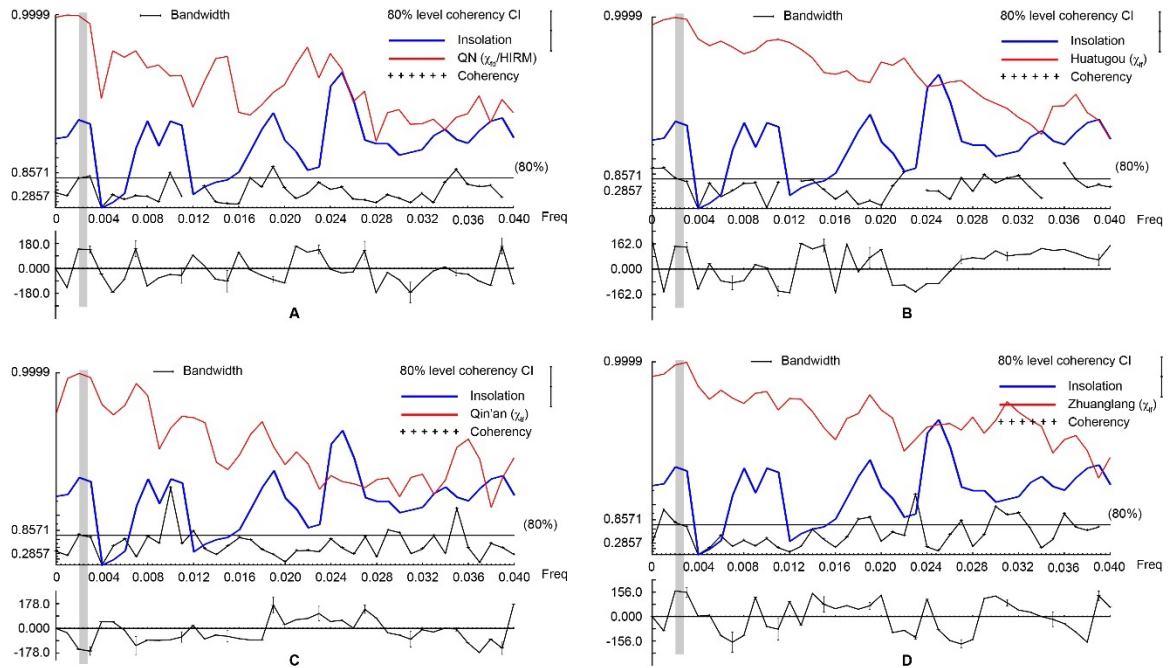


Figure S10. Environmental magnetic parameter variations of QN section during the middle Miocene. (A) χ_{fd}/HIRM . (B) χ_{fd} . (C) Eccentricity (Laskar et al., 2004). (D) Benthic

153 $\delta^{18}\text{O}$ stack (Westerhold et al., 2020). The dashed lines in A, B, C and D are their 405 kyr
 154 components.

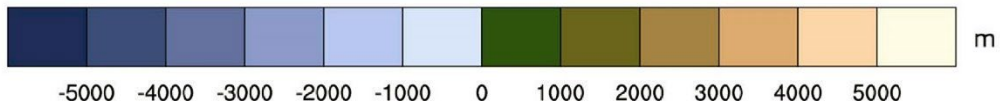
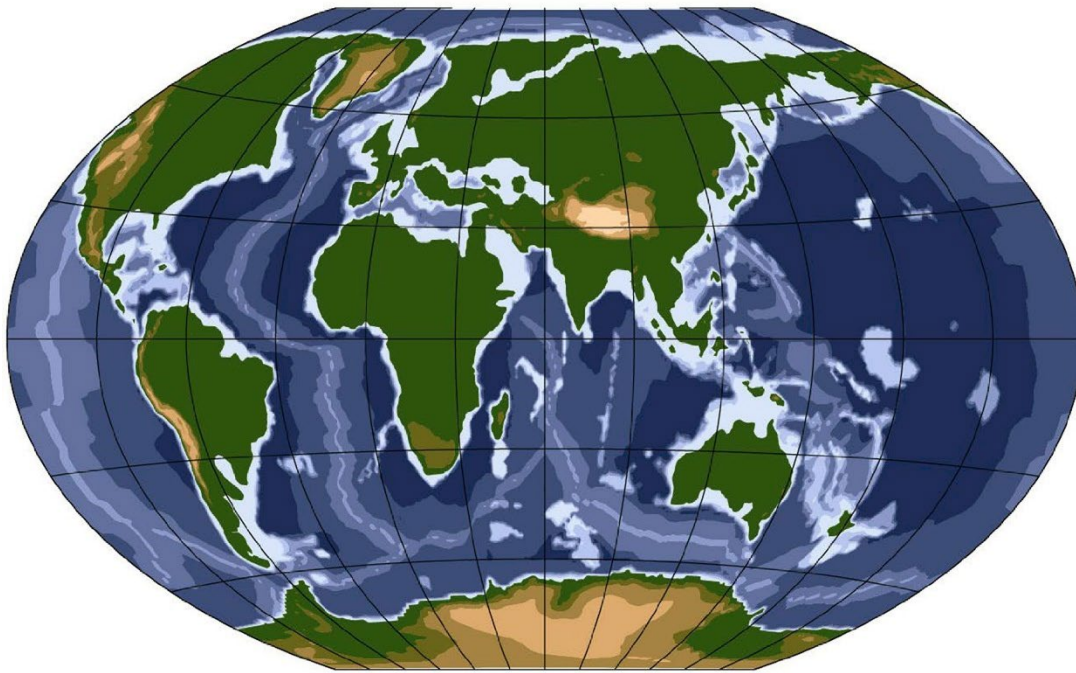
155



156

157 **Figure S11. Cross-spectral analyses between insolation and paleoclimate records in**
 158 **inland Asia during the MMCO (14-17 Ma).** These plots show the coherence and phase
 159 between insolation and the QN section χ_{fd} /HIRM records (A), Huatugou χ_{lf} records (B),
 160 Qin'an χ_{lf} records (C), and Zhuanglang χ_{lf} records (D). Spectral densities are normalized
 161 and plotted on a log scale. The analyses were performed by “ARAND” software (Howell
 162 et al., 2006). Before analyses, the data were interpolated at 2-kyr steps. The coherence
 163 spectra are plotted on a hyperbolic arctangent scale. The horizontal lines show the nonzero
 164 coherence at the 80% statistical confidence level. The shaded vertical bars indicate the
 165 range of the 405-kyr orbital cycles.

166



167

168 **Figure S12. Paleogeographic reconstruction used in the middle Miocene simulations**

169 **(Poblete et al., 2021).**

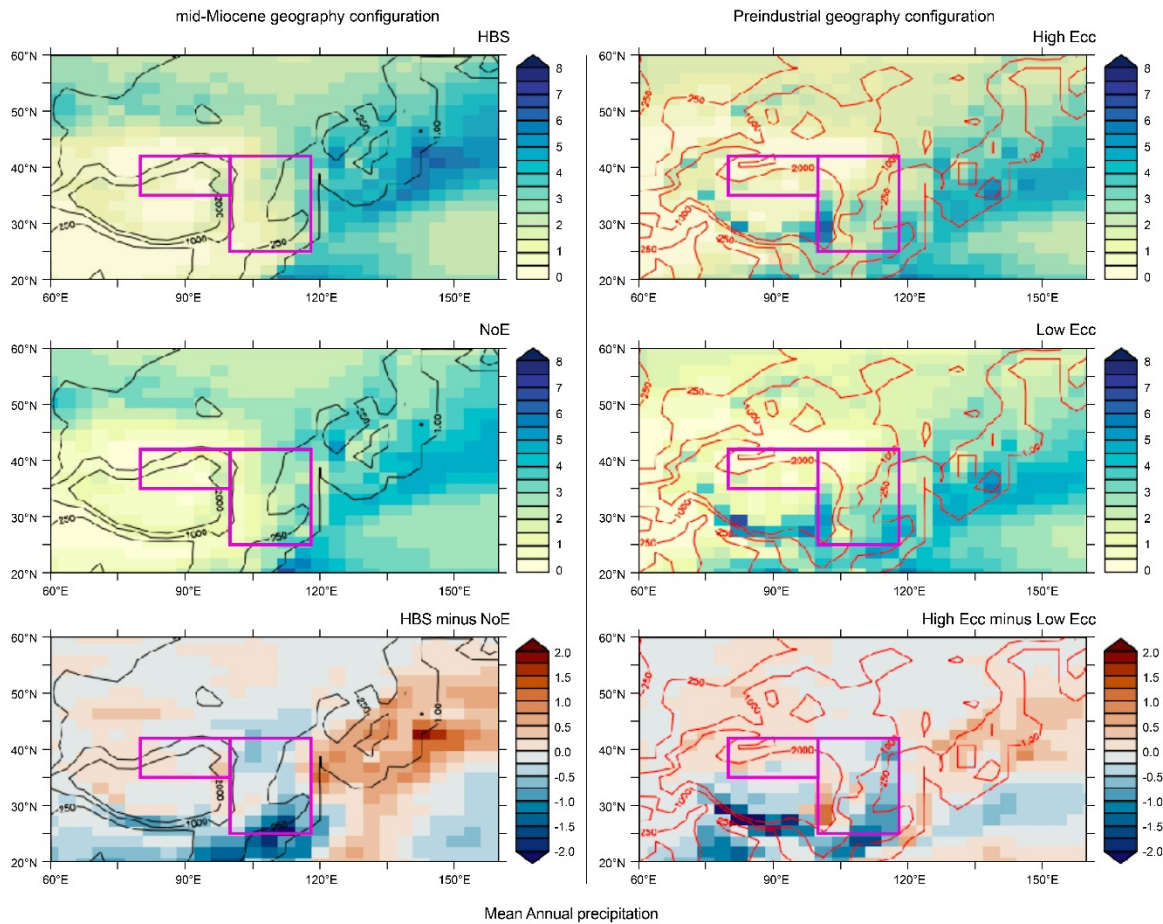


Figure S13. Changes in mean annual precipitation (shaded, mmday^{-1}) in response to Earth's orbit eccentricity. The left/right panel illustrates the precipitation changes during periods of high eccentricity, low eccentricity, and their difference (high eccentricity precipitation minus low eccentricity precipitation) under the mid-Miocene/Preindustrial geographical configuration (see Climate simulations section for description of the mid-Miocene setups). Pre-industrial simulation parameters are from Beaufort et al. (2022). The purple rectangles represent the rough locations of the Northeastern Tibetan Plateau and East Asia. The Earth orbital parameters used for the simulation are shown in Table S7.

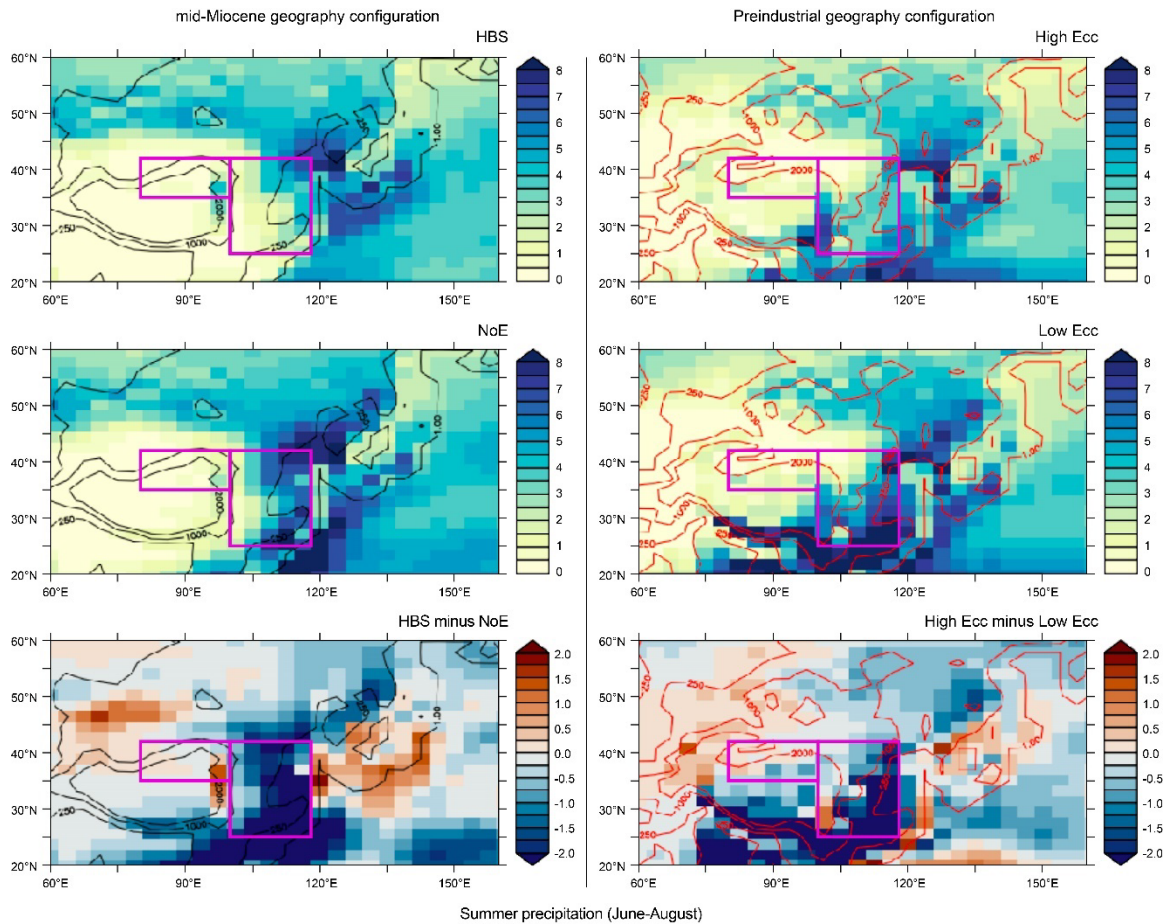


Figure S14. Changes in summer precipitation (shaded, mmday^{-1}) in response to Earth's orbit eccentricity. The left/right panel illustrates the precipitation changes during periods of high eccentricity, low eccentricity, and their difference (high eccentricity precipitation minus low eccentricity precipitation) under the mid-Miocene/Preindustrial geographical configuration (see Climate simulations section for description of the mid-Miocene setups). Pre-industrial simulation parameters are from Beaufort et al. (2022). The purple rectangles represent the rough locations of the Northeastern Tibetan Plateau and East Asia. The Earth orbital parameters used for the simulation are shown in Table S7.

REFERENCES CITED

- Beaufort, L., Bolton, C. T., Sarr, A. C., Sucheras-Marx, B., Rosenthal, Y., Donnadieu, Y., Barbarin, N., Bova, S., Cornuault, P., Gally, Y., Gray, E., Mazur, J. C., and Tetard, M., 2022, Cyclic evolution of phytoplankton forced by changes in tropical seasonality: *Nature*, v. 601, no. 7891, p. 79-+.
- Grinsted, A., Moore, J. C., and Jevrejeva, S., 2004, Application of the cross wavelet transform and wavelet coherence to geophysical time series: *Nonlinear Processes in Geophysics*, v. 11, no. 5-6, p. 561-566.
- Howell, P., Pisias, N., Ballance, J., Baughman, J., and Ochs, L., 2006, ARAND Time-Series Analysis Software, Brown University, Providence RI.
- Lallier, F., Antoine, C., Charreau, J., Caumon, G., and Ruiju, J., 2013, Management of ambiguities in magnetostratigraphic correlation: *Earth and Planetary Science Letters*, v. 371, p. 26-36.
- Laskar, J., Robutel, P., Joutel, F., Gastineau, M., Correia, A. C. M., and Levrard, B., 2004, A long-term numerical solution for the insolation quantities of the Earth: *Astronomy & Astrophysics*, v. 428, no. 1, p. 261-285.
- Ogg, J., 2020, Geomagnetic polarity time scale, *Geologic time scale 2020*, Elsevier, p. 159-192.
- Poblete, F., Dupont-Nivet, G., Licht, A., van Hinsbergen, D. J. J., Roperch, P., Mihalynuk, M. G., Johnston, S. T., Guillocheau, F., Baby, G., Fluteau, F., Robin, C., van der Linden, T. J. M., Ruiz, D., and Baatsen, M. L. J., 2021, Towards interactive global

211 paleogeographic maps, new reconstructions at 60, 40 and 20 Ma: Earth-Science
212 Reviews, v. 214.

213 Tauxe, L., and Gallet, Y., 1991, A Jackknife for Magnetostratigraphy: Geophysical
214 Research Letters, v. 18, no. 9, p. 1783-1786.

215 Westerhold, T., Marwan, N., Drury, A. J., Liebrand, D., Agnini, C., Anagnostou, E., Barnet,
216 J. S. K., Bohaty, S. M., De Vleeschouwer, D., Florindo, F., Frederichs, T., Hodell,
217 D. A., Holbourn, A. E., Kroon, D., Laetano, V., Littler, K., Lourens, L. J., Lyle,
218 M., Palike, H., Rohl, U., Tian, J., Wilkens, R. H., Wilson, P. A., and Zachos, J. C.,
219 2020, An astronomically dated record of Earth's climate and its predictability over
220 the last 66 million years: Science, v. 369, no. 6509, p. 1383-+.

221 Yin, A., Dang, Y. Q., Zhang, M., Chen, X. H., and McRivette, M. W., 2008, Cenozoic
222 tectonic evolution of the Qaidam basin and its surrounding regions (Part 3):
223 Structural geology, sedimentation, and regional tectonic reconstruction: Geological
224 Society of America Bulletin, v. 120, no. 7-8, p. 847-876.

225 Zijdeveld, J., 1967, A. C. demagnetization of rocks: Analysis of results: Method in
226 Palaeomagnetism.

227

U-Pb zircon dating methods at CEREGE (2022-2023)

Analytical Set-up

Our laser ablation system is an ESI laser (ArF 193 nm) equipped with a 25x25 cm sample cell and controlled with AV2 software. The ablated material is carried in helium into the plasma source of an Element XR HR-ICP-MS, operating with a standard quartz torch, with a nickel sample cone and a nickel H skimmer cone the skimmer cone. Our analytical set-up is summarized in Table 1 (following the reporting template of Horstwood et al., 2016). The He carrier gas passes through a Hg trap (model MS-T700-2 of VICI Mat/Sen) before entering the sample cell to maintain a low Hg background. For a given laser spot diameter (25 microns), the main laser parameters (carrier gas flows, fluence, repetition rate), analyte dwell times, and work flow timing (acquisition and wash-out duration) were determined by performing line scans on NIST SRM 612 reference material glass and shooting a set of international zircon reference materials (Table 2) while monitoring the stability and sensitivity of ^{238}U , ^{232}Th and ^{206}Pb . We opted for 15 Hz pulse repetition rate, an energy fluence of 1.5 J cm^{-2} and a carrier gas flow of 0.975 L/min . Monitored masses include ^{202}Hg , ^{238}U , ^{235}U , ^{232}Th , ^{208}Pb , ^{207}Pb , ^{206}Pb , and ^{204}Pb , analyzed over 4 mass windows (100 samples per peak for every mass) in both analog and pulse-counting modes, with a total, combined dwell time of $\sim 0.373 \text{ s}$.

While laser parameters remain unchanged over time, our ICP-MS instrument is manually tuned daily in order to yield Th/U ratios close to unity (typically between 1 and 1.25) on line scans of NIST SRM 612 reference material glass, while keeping ^{238}U sensitivity high.

Analytical workflow

Zircon crystals are extracted from 1 to 5 kg samples by traditional methods of crushing and grinding, followed by a 3-step separation sequence with a Wilfley table, heavy liquids, and a Frantz magnetic separator. A split of 100 to 1000 zircon crystals is separated (without sieving, to include all grain sizes) and incorporated into a 1" epoxy mount together with fragments of our zircon reference materials. We use the 91500 international standard zircon, dated by CA-ID-TIMS at 1065.4 ± 0.3 (2σ) Myr (Wiedenbeck et al., 1995) as our primary reference material, and commonly two out of three secondary reference materials that we have in great quantity: GHB, our internal standard available at request, coming from the Hypersolvus granite of the Golden Horn Batholith of the North Cascades, and dated by CA-ID-TIMS at 48.205 ± 0.060 (2σ) Myr (Eddy et al., 2016); FC-1, from the Duluth gabbro complex in Minnesota, dated at $1,099.5 \pm 0.33$ (2σ) Myr by ID-TIMS (Paces and Miller, 1993); and Plesovice, coming from granulite facies of the Bohemian Massif in the Czech Republic, dated at 337.13 ± 0.37 (2σ) Myr (Slama et al., 2008). If needed (for example, if other minerals can be visually identified in the heavy mineral extracts), mounts are imaged with a backscattered electron detector (BSE) with a ZEISS EVO 15 LSM710 Scanning Electron Microscope (SEM) to distinguish zircons from other remaining heavy minerals. Mounts are polished prior to isotopic analysis.

Once epoxy mounts are loaded in the laser ablation cell, all zircons (standards and unknowns) are pre-ablated before the analytical session (only 2 ablations with a laser spot diameter at 40 microns, fluence of 2.4 J/cm^2). A laser ablation pass involves (1) a single 3-s carrier gas blank with no laser firing, (2) 13 s of laser ablation, and (3) 14 s of washout time with no laser firing to allow all sample material to purge through the system and to prepare for the next analysis. Ions generated by the ablation take ca. 3 s to reach the SEM detectors.

Each individual data acquisition on the Element XR consists of 17.5 s of measurement during which the mass spectrometer completes 47 sweeps through the 202 to 238 mass range. Initiation of data acquisition by the Element XR is triggered externally by the laser system. The first ca. 6 s of acquisition (approx. 15 sweeps) cover the 3 s gas blank with the laser off and the additional 3 s delay for the arrival of ablated material to the detector. The remaining time (and sweeps) covers the window when ablated material reach the SEM detectors. A session starts and ends with seven 91500 standards; additionally, we shoot the "91500" standard or a secondary standard every 5 unknowns. This yields a throughput of 80 unknown zircons analysed per hour.

Table 1: Summary of analytical set-up

Laboratory & Sample Preparation	
Laboratory name	ENVITOP, CEREGE, Aix-Marseille Université
Sample type/mineral	Zircons
Sample preparation	Conventional mineral separation, 1-inch resin mount, 3µm polish to finish
Imaging	ZEISS EVO 15 LSM710 Scanning Electron Microscope
Laser ablation system	
Make, Model & type	ESI 193 nm
Ablation cell	15x15 cm
Laser wavelength (nm)	193 nm
Pulse width (ns)	< 5 ns
Fluence (J.cm ⁻²)	1.2 J.cm ⁻²
Repetition rate (Hz)	15 Hz
Ablation duration (s)	13 seconds
Ablation pit depth / ablation rate	10.5 µm pit depth, measured using a profilometer, equivalent to 0.05µm/pulse
Spot diameter (µm) nominal/actual	25 µm / 27 µm
Sampling mode / pattern	Static spot ablation
Carrier gas	100% He in the cell
Cell carrier gas flow (l/min)	0.900 to 0.975 L/min for He
ICP-MS Instrument	
Make, Model & type	Element XR, HR-ICP-MS
Sample introduction	Ablation aerosol
RF power (W)	1200W
Make-up gas flow (l/min)	Cool flow 16 L/min, Auxiliary gas flow 0.75-0.85 L/min, sample gas flow 1 L/min
Detection system	Dual mode (ion counting and analogue) secondary electron multiplier (SEM)
Masses measured	202Hg, 204Pb, 206-208Pb, 232Th, 235U, 238U
Integration time per peak/dwell times (ms); quadrupole settling time between mass jumps	202Hg: 0.005s, 204Pb: 0.0078s, 206Pb: 0.02s, 207Pb: 0.028s, 208Pb: 0.0025s, 232Th: 0.0025s, 235U: 0.0154s, 238U: 0.101s
Total integration time per output datapoint	0.373s
'Sensitivity' as useful yield (% , element)	0.2% U
ICP-MS Dead time (ns)	25 ns
Data Processing	
Gas blank	3 seconds on-peak zero subtracted
Calibration strategy	91500 used as primary reference material, GHB, Plesovice and FC-1 used as secondaries/validation
Reference Material info	91500 (Wiedenbeck et al. 1995) Plesovice (Slama et al. 2008) GHB (Eddy et al. 2016) FC-1 (Paces and Miller, 1993)
Data processing package used / Correction for LIEF	in-house Matlab algorithm (cf main text)
Mass discrimination	NIST612 used for initial mass bias correction during autotuning, then 207Pb/206Pb and 206Pb/238U normalised to reference material
Common-Pb correction, composition and uncertainty	Common-Pb correction applied to the data using 204Pb correction based on Stacey and Kramers (1985) isotopic ratios.
Uncertainty level & propagation	Ratio are quoted at 2s percentage, Ages are quoted at 2s absolute, propagation is by quadratic addition.
Quality control / Validation	Cf Table 2 and Figure 2b.

Data processing

data importing and isotope Ratio calculation

Raw data from the instrument were decoded using *ExtractDat* (Hartman et al., 2017) to provide counts per second for ion beam intensities of both detection modes. All the following data reduction steps are done with our in-house Matlab script, *Age_Redux*, built from the Matlab code of *AgeCalcML* (<https://www.kurtsundell.com/agecalcml>), the data reduction software from the Arizona Laserchron Center. *Age_Redux* allows multiple ways and options to calculate isotope ratios, ages and their uncertainties, and enables a direct comparison between data reduction protocols.

For every sweep, beam intensity for each mass is calculated as the sum over the 4 mass windows. On-peak background intensity is calculated by averaging the beam intensity over all sweeps before the arrival of ablated material to the SEM detector. The delay of arrival can vary by \pm one sweep, so we automatically detect the arrival of ablated material to the SEM detector while looking at the maximum of the total beam intensity derivative. The integration window for individual beam intensities has a fixed width (30 sweeps); as the five sweeps following the arrival of ablated material typically have high signal transience, the integration window starts at the 6th sweep after this arrival.

The calculation of ^{238}U beam intensity is often challenging because of the high amount of uranium in young zircons, resulting in frequent shifts from ion counting mode to analogue mode. We tested several methods to homogenize the calculation of the ^{238}U beam intensity through a session. Using ^{235}U to calculate ^{238}U with a 137.818 scaling factor (Hiess et al., 2012) yields accurate and precise results for secondary reference materials when the beam intensity is high but decreases the precision of calculated $^{206}\text{Pb}/^{238}\text{U}$ ratio at low beam intensity. We opted for a hybrid method of using ^{235}U to calculate ^{238}U above an ion count threshold ($^{238}\text{U} > 2\,000\,000$ cps), and raw ^{238}U ion counts below this threshold. Our tests show that this method yields a similar precision for isotopic ratios at both high and low ^{238}U beam intensity, and that it reduces the scatter between individual reference materials when compared with the ACF (analogue conversion factor) approach proposed by Pullen et al. (2018), that converts analogue counting outputs into an equivalent number of counts.

We tested five approaches commonly used to calculate U-Pb isotope ratios over each integration window: the ratio of the average background-corrected beam intensities (the "ratio of the mean" approach, opted by Pullen et al., 2018); the average of isotopic ratios calculated from background-corrected beam intensities (the "mean of the ratios" approach); the intercept method applied on the same isotopic ratios (the "traditional intercept" approach, sensu Fisher et al. 2010); the additive log-ratio transform of the isotopic ratios ("the log-intercept" approach of McLean et al. 2016); and the intercept method applied to the additive log-ratio transform of the isotopic ratios (introduced by McLean et al. 2016). We estimated the precision and accuracy of the five methods by comparing the resulting ages and age uncertainties (see next section for their calculation) for the three secondary reference materials, as well as for a set of additional reference materials at our disposal (Temora2, R33, Oracle, Tan-Bra and OG-1; for ages and characteristics of these zircons, see Pullen et al., 2018 and table 2). We found no significant difference in the accuracy of the five methods; the two intercept approaches yet result in wider random uncertainties and thus lower precision. We opted for the "ratio of the mean" approach as it minimizes the impact of downhole fractionation on the calculated ratios (Pullen et al., 2018).

Detector dead time is known to be a main contributor to measurement bias in the pulse-counting range (Vanhaecke, 2012; Vanhaecke et al., 1998). A Detector dead time correction (of 25 ns) was applied to correct the baseline-corrected beam intensity measured during LA experiments, similar to Pullen et al. (2018).

Fractionation and common lead correction

Instrumental mass and inter-element biases for session-wide drift of $^{206}\text{Pb}/^{238}\text{U}$ and $^{206}\text{Pb}/^{207}\text{Pb}$ are corrected using a sliding window fractionation factor (Gehrels et al., 2008), calculated as a running average of the nearest six primary reference materials that bracket any given analysis (i.e., three prior to the analysis and three after). We commonly notice \pm 2-3% of drift over a 4h session. Outliers in primary reference material analyses are rare and commonly result from misplaced spots during laser spot selection. Two options to remove them are available: they are either manually rejected or automatically detected and rejected when their isotopic ratio deviates from $>10\%$ of their expected, drift-corrected ratio.

We calculate $^{206}\text{Pb}/^{238}\text{U}(\ast)$ and $^{206}\text{Pb}/^{207}\text{Pb}(\ast)$ ratios corrected for initial lead using the ^{204}Pb -based

method (e.g. Mattinson, 1987). This method assumes a unique Pb isotopic composition for initial lead (Stacey and Kramers, 1975), uses measured ^{204}Pb to estimate the amount of initial ^{206}Pb and ^{207}Pb , and corrects $^{206}\text{Pb}/^{238}\text{U}$ and $^{206}\text{Pb}/^{207}\text{Pb}$ based on this estimate and the assumed isotopic composition. Measured ^{204}Pb is obtained by subtracting background ^{204}Hg and ^{204}Pb on mass 204; background ^{204}Hg is obtained from mass 202 by using a natural $^{202}\text{Hg}/^{204}\text{Hg}$ ratio of 4.3 (Rosman and Taylor, 1998). The calculation of $^{206}\text{Pb}/^{238}\text{U}^*$ and $^{206}\text{Pb}/^{207}\text{Pb}^*$ ratios is done after the correction for instrumental mass drift. Note that we recalculate the correction for instrumental drift after this step, using the $^{206}\text{Pb}/^{238}\text{U}^*$ and $^{206}\text{Pb}/^{207}\text{Pb}^*$ of the primary reference material.

Pullen et al. (2018) noted a systematic bias in the isotopic ratios of reference material at low and high ^{238}U beam intensity, that they correct using an empirically-determined scaling factor. We do not observe such bias in our results (Fig. 1a), and such correction is not thus applied.

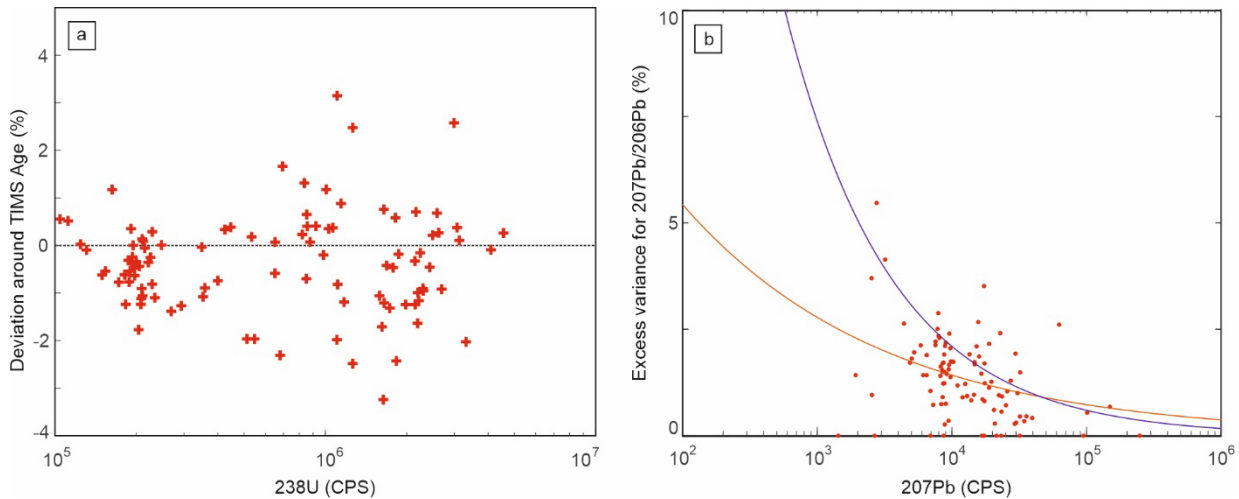


Figure 1. (a) Deviation around the TIMS age of reference materials (weighted mean per session, over 54 sessions) compared to their measured ^{238}U (in cps). **(b)** Excess variation for $^{207}\text{Pb}/^{206}\text{Pb}$ calculated for reference materials over one year of analysis ($n=107$) compared to their measured ^{207}Pb (in cps), and power curve best-fit line across all sessions (red curve; $y = 9.2647 * x^{-0.2326}$, $r^2=0.6$); in blue, the best-fit line of Matthew and Guest (2017).

Internal uncertainty, excess variance and other sources of uncertainties

The calculation of internal uncertainty (in %) for all ratios is made following the protocol defined by Pullen et al. (2018). For pairs that do not experience down-pit fractionation, such as $^{206}\text{Pb}/^{204}\text{Pb}$ and $^{206}\text{Pb}/^{207}\text{Pb}$, the uncertainty is calculated as the standard deviation of the ratio over the integration window. The uncertainty for $^{206}\text{Pb}/^{238}\text{U}$ is determined as the uncertainty of an unweighted least squares linear regression through the changing ratios over the integration window (standard error of the intercept).

The uncertainty generated by the common lead correction is calculated following Mattinson (1987) and is added to the internal uncertainty by quadratic sum.

Excess variance in $^{206}\text{Pb}/^{238}\text{U}^*$ ratio for each session is determined on the replicate measurements of our primary reference material. The excess variance, additional to the measurement uncertainty required to give the population an MSWD of 1, is determined on all measurements. This excess variance is then quadratically added to internal uncertainty of the $^{206}\text{Pb}/^{238}\text{U}$ ratios for all unknowns to generate the random uncertainty.

Excess variance in the $^{207}\text{Pb}/^{206}\text{Pb}^*$ ratio is complicated by the variable and low beam intensity for ^{207}Pb in many zircons (Horstwood et al., 2016). To account for this, we developed a multi-session calibration curve based on one year of analysis (107 analyzes of reference material). Excess variance was calculated for every primary and secondary reference materials we used per session, and plotted against their average ^{207}Pb beam intensity per session (Fig. 1b). In most sessions, excess variance decreased from $> 5\%$ to $< 2\%$ for ^{207}Pb cps between 500 and 5000, similar to what is reported by Horstwood et al. (2003) and Matthew and Guest (2017). A power curve best-fit line (Fig. 1b) yields a very similar shape than the one determined by Matthew and Guest (2017), and serves as the excess variance calibration curve. To determine the excess variance calibration curve for each individual session, this power curve best-fit line is multiplied

by a correction factor calculated by minimizing the misfit between the curve and the excess variance of the primary and secondary standard(s) measured during that session. The excess variance is then calculated for every unknown based on the corrected power curve best-fit line, and quadratically added to internal uncertainty to calculate random uncertainties. Note that we do not proceed to a 2-s outlier rejection when calculating the MSWD, unlike how *Iolite* data reduction schemes proceed (Paton et al., 2010); our excess variance and resulting random uncertainty for the 207Pb/206Pb ratio are thus conservative estimates.

Over one year of analysis (n=8,607), measurement uncertainties in 206Pb/238U ages result in a 2 to 5% random uncertainty (at 2-sigma), with an average at 3.3 % for ages younger than 500 Ma and 2.6% for ages older than 2000 Ma. The random uncertainty in 207Pb/206Pb ages is substantially larger for younger grains due to low intensity of the 207Pb signal, but decrease below 2% above 2.5 Ga (Fig. 2a).

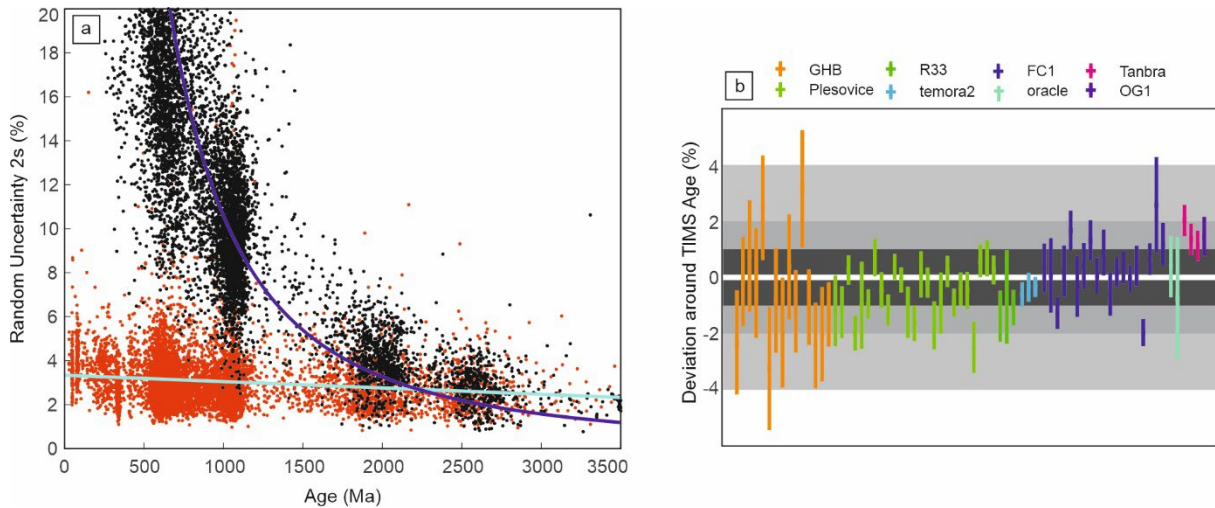


Figure 2. (a) Random uncertainty in 206Pb/238U ages (red dots) and 207Pb/206Pb ages (black dots); Solid blue line is a linear regression for 206Pb/238U ages, solid purple line is a power law fit for the 206Pb/207Pb ages. (b) Deviation around the published TIMS age for ten secondary reference materials (details in Table 2). Horizontal bars correspond to the weighted mean \pm 2 random uncertainty (and thus not including the systematic uncertainty) for individual sessions with more than n= 5 analyses per secondary standard.

Accuracy, systematic uncertainty, and comparison with other approaches

The accuracy of approach can be evaluated while looking at Concordia ages of our secondary reference material, displayed on Fig. 2b. Most ages for secondary material display less than 2% of deviation around their TIMS age, and very often within 1 % of deviation (Fig. 2b). The accuracy over multiple sessions is analogous to what is found with MC- and SD-ICP-MS (Gehrels et al., 2008; Pullen et al., 2018).

Table 2: MSWD and Excess variance calculated for eight secondary reference materials over one year of analysis.

Reference materials						206Pb/238U ratio		207Pb/206Pb ratio	
Name	206Pb*/238U age (Ma, ± 2σ)	206Pb*/207Pb* age (Ma, ± 2σ)	Technique	Reference	number of analysis	MSWD	Excess variance (2s, in %)	MSWD	Excess variance (2s, in %)
GHB	48.205 ± 0.060	N/A	CA-ID-TIMS	Eddy et al. (2016)	55	2.9	2.8	0.6	0
Plesovice	337.1 ± 0.2	339.3 ± 0.3	ID-TIMS	Sláma et al. (2008), Horstwood et al. (2016)	709	1.6	1.3	0.9	0
temora2	416.78 ± 0.33	420.13 ± 0.30	ID-TIMS & CA-TIMS	Black et al. (2004), Mattinson (2010)	39	1.8	1.7	1.1	1.1
R33	419.3 ± 0.4	422.37 ± 0.36	ID-TIMS & CA-TIMS	Black et al. (2004), Mattinson (2010)	45	1.8	1.7	1.4	1.8
FC1	1,099.5 ± 0.33	1,099.0 ± 0.16	ID-TIMS	Paces and Miller (1993)	408	2.7	2.4	1.1	0.7
oracle	1,436.2 ± 1.3	1,437.4 ± 0.77	CA-TIMS	Bowring (Communication in Pullen et al., 2018)	15	2.4	2.3	0.4	0
Tanbra	2,507.8 ± 1.5	2,512.24 ± 0.71	CA-TIMS	Pecha (Communication in Pullen et al., 2018)	35	2.7	2.8	1.2	1.2
OG1	3,440.7 ± 3.2	3,465.4 ± 0.6	ID-TIMS	Stern et al. (2009)	26	1.3	1.1	1.1	0.6

Systematic uncertainties are calculated following recommendations of Hortswood et al. (2016) by quadratically adding (1) the uncertainty in the ratio of our “91500” primary reference material (Wiedenbeck et al., 1995); (2) the uncertainty in the decay constants (Jaffey et al. 1971, following modifications by Mattinson, 1987) and (3) the long-term excess variance around secondary reference materials. The long-term excess variance in 206Pb/238U is variable between the secondary reference materials we used, likely reflecting matrix effects, and varying 207Pb sensitivity between sessions which differently affects young and old zircons. We use the excess variance in 206Pb/238U for reference material Plesovice (1.3 %, 2 σ) as a proxy for the systematic uncertainty in 206Pb/238U, and the excess variance in 207Pb/206Pb ratios for reference material FC1 (0.7 %, 2 σ) as a proxy for the systematic uncertainty in 207Pb/206Pb, as both are the youngest and oldest reference materials for which we have the most analyzes (n=709 and 408 respectively). Using these two values for the systematic uncertainty, the MSWD around the weighted age of secondary reference materials falls between 0.7 and 1.8, with an average of 1.1. Results for all secondary reference materials are given in Table 2, and Total systematic uncertainties are reported in Table 3.

Table 3: Calculated systematic uncertainty for 206Pb/238U and 207Pb/206Pb ratios. See main text for details.

	Uncertainty in 91500 Std, 2s (in %)	Uncertainty in Decay constants, 2s (in %)	long-term excess variance in FC1 and Plesovice reference material, 2s (in %)	Total systematic uncertainty, 2s (in %)
reference	Wiedenbeck et al., 1995	Mattinson, 1987	here	
206Pb/238U ratio	0.089	0.16	1.3	1.31
207Pb/206Pb ratio	0.027	0.26	0.7	0.75

Our procedure diverges from the one described by Pullen et al. (2018) for the LaserChron facility at the University of Arizona on three main points: (1) the calculation of the measured (ACF-corrected for the LaserChron, 235U-based here); (2) the correction for biases at high and low beam intensity (empirically determined at the LaserChron; absent here); (3) the calculation and addition of the excess variance to the internal uncertainty (absent at the LaserChron; done here, following Matthew and Guest, 2017). Adding the excess variance to the procedure of Pullen et al. (2018) significantly decreases the resulting precision, with random uncertainties between 2 to 5% (vs 1 to 4 % at the LaserChron facility). However, our approach yields particularly low systematic uncertainties, which compensate the higher random uncertainties (see table 3).

We also compared the ratios, ages and uncertainties obtained by our procedures with the same ones using *Iolite* software and their *U_Pb_Geochron4* Data Reduction Scheme to get U-Pb ages (Paton et al., 2010). *Iolite* is not designed to take into account mass spectrometers with different SEM detectors; we found overall no discrepancy between results of both approaches.

Determination of the best age for individual zircons

Sedimentary provenance studies using zircon geochronology commonly look at age distributions of individual zircons. Given the relative imprecision of the 235U and 207Pb measurements in LA-ICP-MS, the 207Pb/235U age is rarely used in interpretations and is primarily used to measure the discordance of an analysis (Spencer et al., 2016); there are thus effectively two isotopic ages (206Pb/238U, and 207Pb/206Pb) from which the ‘best age’ of an individual zircon is chosen. It is common practice to use the 207Pb/206Pb age for zircons older than a lab-dependent age threshold (1.0 to 2.5 Gyr) and to use 206Pb/238U ages for those younger. Our laboratory-dependent age cut-off is 2.2 Gyr, above which the random uncertainty in 207Pb/206Pb ages becomes lower than the one for 206Pb/238U ages (see Fig. 1a). Recently, Vermeesch (2021) recommended the use of the Concordia age for single grains, a hybrid age that considers both isotopic ratio composition and its analytical uncertainty, calculated by “projecting” both ratios on the Concordia curve in Wetherill or Tera-Wasserburg space. We opted for this approach (in Wetherill space) after comparing the resulting single grain ages for individual secondary reference materials: resulting Concordia ages are generally more accurate than 206Pb/238U, and 207Pb/206Pb ages, as noticed by Vermeesch (2021).

As individual zircon ages can be influenced by lead loss and by inadequate/incomplete corrections for common lead, zircon ages are screened for concordance before use in the data set. This is generally quantified either by using the ratio of the $^{206}\text{Pb}/^{238}\text{U}$ and $^{207}\text{Pb}/^{206}\text{Pb}$ ages only, for all grains (Gehrels et al., 2011) or only old grains (Licht et al., 2018), or by using the ratio of the $^{206}\text{Pb}/^{238}\text{U}$ and $^{207}\text{Pb}/^{206}\text{Pb}$ above an age threshold and the ratio between the $^{206}\text{Pb}/^{238}\text{U}$ and $^{207}\text{Pb}/^{235}\text{U}$ ages below (Spencer et al., 2014). There is no community-based agreement or rigorous method on how to measure the discordance for individual grains and how to rigorously establish age thresholds if a change in discordance index is needed (Nemchin and Cawood, 2005; Spencer et al., 2016). We follow here the recommendation of Vermeesch (2021), that uses the distance to the concordia line to estimate the degree of discordance for individual grains. This use is coherent with our choice of the Concordia Age for the best zircon age. We use a 10% discordance filter and -5% for reverse discordance, roughly corresponding to a 20% (resp. -10%) filter using the ratio of the $^{206}\text{Pb}/^{238}\text{U}$ and $^{207}\text{Pb}/^{206}\text{Pb}$ ages according to our observations.

References

- Black, L. P., Kamo, S. L., Allen, C. M., Davis, D. W., Aleinikoff, J. N., Valley, J. W., ... & Foudoulis, C. (2004). Improved $^{206}\text{Pb}/^{238}\text{U}$ microprobe geochronology by the monitoring of a trace-element-related matrix effect; SHRIMP, ID-TIMS, ELA-ICP-MS and oxygen isotope documentation for a series of zircon standards. *Chemical Geology*, 205(1-2), 115-140.
- Eddy, M. P., Bowring, S. A., Miller, R. B., & Tepper, J. H. (2016). Rapid assembly and crystallization of a fossil large-volume silicic magma chamber. *Geology*, 44(4), 331-334.
- Gehrels, G. E., Valencia, V. A., & Ruiz, J. (2008). Enhanced precision, accuracy, efficiency, and spatial resolution of U-Pb ages by laser ablation-multicollector-inductively coupled plasma-mass spectrometry. *Geochemistry, Geophysics, Geosystems*, 9(3).
- Gehrels, G., Kapp, P., DeCelles, P., Pullen, A., Blakey, R., Weislogel, A., ... & Yin, A. (2011). Detrital zircon geochronology of pre-Tertiary strata in the Tibetan-Himalayan orogen. *Tectonics*, 30(5).
- Hiess, J., Condon, D. J., McLean, N., & Noble, S. R. (2012). $^{238}\text{U}/^{235}\text{U}$ systematics in terrestrial uranium-bearing minerals. *Science*, 335(6076), 1610-1614.
- Horstwood, M. S., Foster, G. L., Parrish, R. R., Noble, S. R., & Nowell, G. M. (2003). Common-Pb corrected in situ U-Pb accessory mineral geochronology by LA-MC-ICP-MS. *Journal of Analytical Atomic Spectrometry*, 18(8), 837-846.
- Horstwood, M. S., Košler, J., Gehrels, G., Jackson, S. E., McLean, N. M., Paton, C., ... & Bowring, J. F. (2016). Community-derived standards for LA-ICP-MS U-(Th-) Pb geochronology—Uncertainty propagation, age interpretation and data reporting. *Geostandards and Geoanalytical Research*, 40(3), 311-332.
- Jaffey, A. H., Flynn, K. F., Glendenin, L. E., Bentley, W. T., & Essling, A. M. (1971). Precision measurement of half-lives and specific activities of U 235 and U 238. *Physical review C*, 4(5), 1889.
- Klepeis, K. A., Crawford, M. L., & Gehrels, G. (1998). Structural history of the crustal-scale Coast shear zone north of Portland Canal, southeast Alaska and British Columbia. *Journal of Structural Geology*, 20(7), 883-904.
- Licht, A., Dupont-Nivet, G., Win, Z., Swe, H. H., Kaythi, M., Roperch, P., ... & Jones, D. (2018). Paleogene evolution of the Burmese forearc basin and implications for the history of India-Asia convergence. *GSA Bulletin*, 131(5-6), 730-748.
- Matthews, W. A., & Guest, B. (2017). A Practical Approach for Collecting Large-n Detrital Zircon U-Pb Data sets by Quadrupole LA-ICP-MS. *Geostandards and Geoanalytical Research*, 41(2), 161-180.
- Mattinson, J. M. (1987). U-Pb ages of zircons: A basic examination of error propagation. *Chemical Geology: Isotope Geoscience Section*, 66(1-2), 151-162.
- Mattinson, J. M. (2010). Analysis of the relative decay constants of ^{235}U and ^{238}U by multi-step CA-TIMS measurements of closed-system natural zircon samples. *Chemical Geology*, 275(3-4), 186-198.
- Nemchin, A. A., & Cawood, P. A. (2005). Discordance of the U-Pb system in detrital zircons: implication for provenance studies of sedimentary rocks. *Sedimentary Geology*, 182(1-4), 143-162.
- Paces, J. B., & Miller Jr, J. D. (1993). Precise U-Pb ages of Duluth complex and related mafic intrusions, northeastern Minnesota: Geochronological insights to physical, petrogenetic, paleomagnetic, and tectonomagmatic processes associated with the 1.1 Ga midcontinent rift system. *Journal of Geophysical Research: Solid Earth*, 98(B8), 13997-14013.
- Paton, C., Woodhead, J., Hellstrom, J., Hergt, J., Greig, A. and Maas, R (2010) Improved laser ablation U-Pb

- zircon geochronology through robust down-hole fractionation correction. *Geochemistry, Geophysics, Geosystems*, 11(3), doi:10.1029/2009GC002618
- Pullen, A., Ibáñez-Mejia, M., Gehrels, G. E., Giesler, D., & Pecha, M. (2018). Optimization of a Laser Ablation-Single Collector-Inductively Coupled Plasma-Mass Spectrometer (Thermo Element 2) for Accurate, Precise, and Efficient Zircon U-Th-Pb Geochronology. *Geochemistry, Geophysics, Geosystems*, 19(10), 3689-3705.
- Rosman, K., & Taylor, P. (1998). Isotopic compositions of the elements 1997 (technical report). *Pure and Applied Chemistry*, 70(1), 217–235.
- Schmitz, M. D., & Bowring, S. A. (2001). U-Pb zircon and titanite systematics of the Fish Canyon Tuff: an assessment of high-precision U-Pb geochronology and its application to young volcanic rocks. *Geochimica et Cosmochimica Acta*, 65(15), 2571-2587.
- Sláma, J., Košler, J., Condon, D. J., Crowley, J. L., Gerdes, A., Hanchar, J. M., ... & Schaltegger, U. (2008). Plešovice zircon—a new natural reference material for U–Pb and Hf isotopic microanalysis. *Chemical Geology*, 249(1-2), 1-35.
- Spencer, C. J., Kirkland, C. L., & Taylor, R. J. (2016). Strategies towards statistically robust interpretations of in situ U–Pb zircon geochronology. *Geoscience Frontiers*, 7(4), 581-589.
- Spencer, C. J., Prave, A. R., Cawood, P. A., & Roberts, N. M. (2014). Detrital zircon geochronology of the Grenville/Llano foreland and basal Sauk Sequence in west Texas, USA. *GSA Bulletin*, 126(7-8), 1117-1128.
- Stern, R. A., Bodorkos, S., Kamo, S. L., Hickman, A. H., & Corfu, F. (2009). Measurement of SIMS instrumental mass fractionation of Pb isotopes during zircon dating. *Geostandards and Geoanalytical Research*, 33(2), 145-168.
- Vermeesch, P. (2021). On the treatment of discordant detrital zircon U–Pb data. *Geochronology*, 3(1), 247-257.
- Wiedenbeck, M. A. P. C., Alle, P., Corfu, F., Griffin, W. L., Meier, M., Oberli, F. V., ... & Spiegel, W. (1995). Three natural zircon standards for U-Th-Pb, Lu-Hf, trace element and REE analyses. *Geostandards newsletter*, 19(1), 1-23.